Dynamics and Instabilities of Collapsed Polymers in Shear Flow

A. Alexander-Katz*,†,‡ and R. R. Netz†

Physics Department, Technical University Munich, 85748 Garching, Germany, and Matiere Molle et Chimie, ESPCI, CNRS, UMR 7167, 10 rue Vauquelin, 75005 Paris, France

Received October 19, 2007; Revised Manuscript Received January 29, 2008

ABSTRACT: The dynamics of collapsed polymers in shear flow is very different from that of sheared polymers in good or Θ-solvent solvents, because cohesive attraction between monomers opposes hydrodynamic drag forces. Using hydrodynamic simulations and scaling arguments, we show that a polymeric globule displays a well-defined stretching transition at a threshold shear rate $\dot{\gamma}^*$. Below this critical shear rate, the chain remains in a slightly deformed but compact state, while for shear rates larger than $\dot{\gamma}^*$ the globule undergoes periodic unfolding−refolding cycles. The mechanism for this shear-induced instability is associated with the presence of thermally excited polymeric protrusions and thus very different from the classical scenario of hydrodynamic instabilities at the interface between two viscous liquids. In fact, it turns out that the critical shear rate depends sensitively on temperature and on the microscopic cutoff length scale, i.e., the monomer size. Our results demonstrate that proper inclusion of hydrodynamic effects is crucial: in the free draining case we find $\dot{\gamma}^* \sim R^{-1}$, where R is the globule radius, while in the experimentally relevant case including hydrodynamic interactions $\dot{\gamma}^* \sim R$. For partial drainage, a crossover between these limits is obtained. The power spectrum of the stretching dynamics for collapsed polymers is very different between the nondraining and free-draining scenarios, in contrast to noncollapsed polymers. The shear viscosity of a dilute solution of collapsed polymers displays a clear signature of the unfolding transition at the critical shear rate and exhibits shear thinning for all shear rates considered. We also propose simple scaling arguments for the shear-induced instability of a planar interface between a polymer melt and a viscous fluid.

I. Introduction

A single polymer in good or Θ-solvent conditions subject to simple shear displays a continuous increase of its average extension with increasing shear rate. For very high shear rates, the extension saturates at about one-half of the contour length.[1] The time-dependent configuration of the polymer exhibits periodic elongation, relaxation, and tumbling, even at relatively small shear rates smaller than the inverse polymer relaxation time.[2,3] This behavior is retained even when the polymer is grafted to a solid substrate.[4] On the other hand, a polymer placed in an elongational flow exhibits an abrupt coil−stretch transition once the strain rate is above a critical value.[5,6] Interestingly, the coil in this case exhibits only small length fluctuations across the transition. This behavior was predicted by de Gennes more than 30 years ago, and he showed the case of simple shear flow to be a marginal case that can be turned into a pronounced transition by adding small additional elongational flow components.[7] On the other hand, the behavior of polymers under bad solvent conditions in shear is quite different and is relevant for the stability of proteins in shear flow.[8] Halperin and Zhulina worked out the equilibrium response of a polymeric globule to an extensional force applied to the polymer ends which exhibits a first-order like stretching transition at a threshold force.[9] Brochard and Buguin considered the case of grafted collapsed polymers in shear and showed that they remain compact below a critical shear rate, while above this critical value the chains display a globule−stretch transition.[10] Both works are based on minimizing the free energy resulting from destabilizing forces on the globule (either due to shear flow or external forces acting on the polymer ends) and the cohesion between polymer blobs. This type of analysis does not carry over easily to the case of an ungrafted globule in shear, since an unconstrained globule relaxes stretching forces by rotating in the flow. Very recently, we have shown that ungrafted collapsed polymers exhibit a quite sharp globule−stretch transition.[11] As turns out, the mechanism for unfolding is different from the aforementioned unfolding of grafted collapsed chains and relies on a nucleation-type instability argument. The core of our stability analysis involves the concept of thermally excited polymeric protrusions extending from the globular surface which are subject to cohesive and hydrodynamic drag forces. The nucleation barrier is overcome when the hydrodynamic drag force acting on a protrusion is larger than the restoring cohesive force, giving rise to the shear rate threshold value $\dot{\gamma}^*$. The value of $\dot{\gamma}^*$ is sensitive to the precise hydrodynamic boundary conditions and discriminates between free-draining and nondraining hydrodynamic boundary conditions. Our results are in accord with experimental studies[12] on globular fibers of the so-called von Willebrand factor (vWF), which is a long multimeric protein that plays a vital role in the context of clotting and coagulation in capillary vessels,[13] and with recent studies on the stability of proteins in shear flows.[8,14,15]

Our analysis is based on a combination of hydrodynamic simulations and scaling-type arguments of a coarse-grained polymer model. In this paper, we extend our previous analysis in different directions. (i) We consider partial drainage where the flow can to a certain degree penetrate into the globular structure. This generalization interpolates between the two limits of free draining and nondraining. (ii) In addition to the spherical geometry, relevant for a single collapsed polymer that forms a globule, we formulate the protrusion-induced instability scaling argument also for a planar interface between a polymeric melt and a solvent phase. (iii) We analyze the power spectral distribution of the polymer extension as obtained in our hydrodynamic simulations. This is relevant to experimental video-microscopy studies. The spectral density of collapsed polymers (bad-solvent regime) in shear turns out to be drastically different from swollen polymers (good-solvent regime). (iv) We compute the viscosity η of a dilute solution of globular polymers. The viscosity exhibits shear thinning behavior with different

* Corresponding author.
† Technical University Munich.
‡ Matiere Molle et Chimie, ESPCI, CNRS.

10.1021/ma702331d CCC: $40.75
Published on Web 04/11/2008

dependency on the shear rate above and below the globule−stretch transition.

The protrusion-induced instability mechanism of the interface between a collapsed polymer phase and a viscous solvent in shear differs from the classical scenario of hydrodynamic instability of an interface in shear in several important aspects: The mechanisms of the hydrodynamic instability of a viscous spherical drop and a planar interface in shear have been worked out a long time ago and are known under the names of Taylor and Kelvin−Helmholtz instabilities, respectively.[16,17] The critical shear rates in both cases do not depend on temperature or any microscopic length scale. In contrast, our results do depend on temperature and the monomer size in a decisive fashion. Our scaling results, backed up and confirmed by our hydrodynamic simulations, demonstrate that once thermally activated interfacial fluctuations in the form of protrusions are included, it is the small length scales that become unstable first in shear. This fact gives the critical shear rate its monomer size dependence. It is important to note that our results by no means invalidate the classical large-scale hydrodynamic instability theories; rather, we suggest that both mechanisms peacefully coexist. It turns out that for interfaces between simple low-viscosity liquids the Taylor or Kelvin−Helmholtz mechanisms are typically dominant. However, for highly viscous drops, relevant for polymeric globules, where the Taylor result implies droplet stability for arbitrarily high shear rates,[17] our thermally assisted protrusion instability mechanism will take over and dominate the resultant behavior. It transpires that interfacial fluctuations become important whenever classical hydrodynamic instability arguments would predict interface stability. In that case, small-scale fluctuations (protrusions) become unstable first and thus dominate the shear response.

II. Simulation Methods

We consider the polymer to be composed of N beads of radius a interacting through a potential U. The dynamics of the ith bead position $\mathbf{r}_i$ is given by the Langevin equation

$$\frac{\partial}{\partial t}\mathbf{r}_i = \mathbf{v}_\infty(\mathbf{r}_i) - \sum_j \boldsymbol{\mu}_{ij}\cdot\nabla_{\mathbf{r}_j}U(t) + \boldsymbol{\xi}_i(t) \tag{1}$$

where $\mathbf{v}_\infty(\mathbf{r})$ is the undisturbed solvent flow profile, $\boldsymbol{\mu}_{ij}$ is a mobility matrix, and $\boldsymbol{\xi}_i$ is a random velocity that satisfies $\langle\boldsymbol{\xi}_i(t)\boldsymbol{\xi}_j(t')\rangle = 2k_BT\boldsymbol{\mu}_{ij}\delta(t - t')$. For simple shear flow the undisturbed flow profile is $\mathbf{v}_\infty(\mathbf{r}) = \dot{\gamma}\hat{z}\hat{\mathbf{x}}$, where $\dot{\gamma}$ is the shear rate, z the height and $\hat{\mathbf{x}}$ the unit vector parallel to the x axis. The hydrodynamic interactions with the underlying fluid are captured through the mobility matrix $\boldsymbol{\mu}_{ij}$. We use two different forms of this matrix: in the free draining (FD) case the matrix is diagonal with $\boldsymbol{\mu}_{ij} = \mu_0\delta_{ij}\mathbf{1}$, where μ_0 is the mobility of a sphere of radius a in a fluid of viscosity η_s, i.e. $\mu_0 = 1/6\pi\eta_s a$. The second case including hydrodynamic interactions (to which we refer throughout the rest of the paper as HI) approximates the mobility matrix by the Rotne−Prager (RP) tensor[18]

$$\frac{\boldsymbol{\mu}_{ij}}{\mu_0} = \begin{cases} \dfrac{3a}{4r_{ij}}\left(\left(1+\dfrac{2a^2}{3r_{ij}^2}\right)1 + \left(1-\dfrac{2a^2}{r_{ij}^2}\right)\dfrac{\mathbf{r}_{ij}\mathbf{r}_{ij}}{r_{ij}^2}\right) & r_{ij} \geq 2a \\ \left(1-\dfrac{9r_{ij}^2}{32a^2}\right)1 + \dfrac{3}{32}\dfrac{\mathbf{r}_{ij}\mathbf{r}_{ij}}{ar_{ij}} & r_{ij} < 2a \end{cases} \tag{2}$$

where $\mathbf{r}_{ij} = \mathbf{r}_i - \mathbf{r}_j$ is the vectorial distance between the ith and jth bead and $r_{ij} = |\mathbf{r}_{ij}|$. Notice that for $i = j$ one obtains the correct limit of the self-mobility of a single particle in unbounded flow, i.e., $\boldsymbol{\mu}_{ij} = \mu_0\mathbf{1}$. The RP tensor is an approximation to the full hydrodynamic interaction between two spheres and accounts to first order for the finite sphere size. Such hydrodynamic simulations have been successful in describing swollen polymers in various flows.[1,6,19,20] By comparing simulations with and without hydrodynamic interactions one can then estimate the importance of hydrodynamic interactions.

The potential energy U is written as $U = U_s + U_{LJ}$. The first term accounts for the connectivity of the chain and is given by

$$U_s = \frac{\kappa}{2}k_BT\sum_{i=1}^{N-1}(r_{i+1,i} - 2a)^2 \tag{3}$$

where $r_{i+1,i}$ is the distance between adjacent beads along the chain, and the spring constant is taken to be $\kappa = 200/a^2$ which limits stretching of the chain to a negligible level. The second term is a Lennard-Jones potential written as

$$U_{LJ} = \tilde{\epsilon}k_BT\sum_{ij}((2a/r_{ij})^{12} - 2(2a/r_{ij})^6) \tag{4}$$

where $\tilde{\epsilon}$ determines the depth of the potential (in units of k_BT). By varying this quantity one can tune the polymer to be swollen (small $\tilde{\epsilon}$) or collapsed (large $\tilde{\epsilon}$). To simulate the dynamics of the polymer in shear flow, we discretize eq 1 and use a time step Δt ranging from $10^{-4}\tau$ to $10^{-6}\tau$, where τ is the characteristic monomer diffusion time $\tau = a^2/\mu_0 k_BT$. Averages are taken over a total number of Langevin steps of at least 2×10^7, with the first 10^6 simulation steps typically discarded for equilibration.

Using the full hydrodynamic matrix not only accounts for hydrodynamic interaction between monomers but also for flow stagnation inside the polymeric globule, as demonstrated in Figure 1), where we show the fluid velocity at position $\mathbf{r}_i$ calculated according to

$$\mathbf{v}(\mathbf{r}_i) = \mathbf{v}_\infty(\mathbf{r}_i) - \sum_j \boldsymbol{\mu}_{ij}\nabla_{\mathbf{r}_j}U \tag{5}$$

inside and outside the globule. The solid-body rotation within the sphere is correctly obtained by our hydrodynamic simulation technique, as is demonstrated by the flow profiles in Figure 1, b and c.

III. Results and Discussion

A. Collapse Transition without Shear. In order to study the dynamics of collapsed polymers, it is first necessary to define the collapse transition point $\tilde{\epsilon}_{col}$ in the absence of shear, i.e., for $\dot{\gamma} = 0$. This transition has been studied previously by theoretical means and by simulations.[21−23] Theoretical considerations based on simple mean field analysis predict a dependence of the collapse or critical point of phase separation $\tilde{\epsilon}_{col}$ of a polymer solution in bad solvent conditions to follow $\tilde{\epsilon}_{col} - \tilde{\epsilon}_\theta \sim N^{-1/2}$, where $\tilde{\epsilon}_\theta$ is the so-called θ-point and corresponds to a value of $\tilde{\epsilon}$ at which repulsive and attractive interactions cancel each other out, and thus ideal-polymer conditions are met. The θ-temperature coincides with the collapse point in the limit $N \rightarrow \infty$ only. The θ temperature has been computed previously for this system using simulations, and it is located at $\tilde{\epsilon}_{col}^{N\rightarrow\infty} = \tilde{\epsilon} \approx 0.314$.[24] This value coincides with our results and corresponds to the point at which the rescaled radii R_g^2/N of different chain length cross (see Figure 2), where $R_g^2 = (1/N)\sum_i(\mathbf{r}_i - \sum_i\mathbf{r}_i)^2$. From this value, one could in principle use the scaling prediction mentioned above and estimate the collapse transition point for finite-length polymers. However, the finite-length scaling prediction only applies to asymptotically long polymers, and in addition the proportionality constant is model dependent, which makes the finite-length scaling prediction useless for the polymer sizes studied in this work. We therefore need to locate the collapse transition based on some observable quantity. Unfortunately, the specific heat or the internal energy does not show a clear sign of the collapse transition for the lengths studied here as the peaks are very small and broad.[22,23] For this reason we define the collapse point $\tilde{\epsilon}_{col}$ as the maximum in the curvature of the radius of gyration, $c = \partial^2\langle R_g^2/Na^2\rangle/\partial\tilde{\epsilon}^2$.

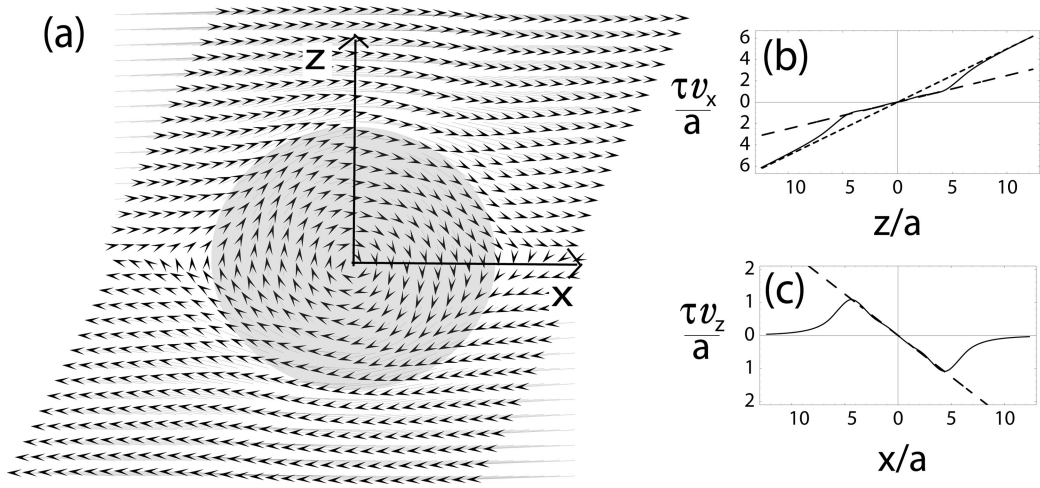

Figure 1. (a) The velocity field in the $x-z$ plane of a strongly collapsed polymer with a radius $R \sim 4.5a$ and $N = 80$ in shear flow. The radius R corresponds to one-half of the extension of the globule along the x axis in the unperturbed case (i.e., $\dot{\gamma} = 0$). The arrows show the direction and the magnitude of the local fluid velocity. The shaded region denotes the globule position and shape. The fluid flow is calculated with respect to the polymer center of mass according to eq 5. (b) The velocity v_x in the x direction as a function of z along a line through the polymer center of mass. The full curve is the calculated velocity profile. The short dashed curve denotes the velocity in the absence of the polymer and has a slope of $\dot{\gamma}\tau$. The long dashed curve corresponds to the rotational velocity of a sphere in shear flow with a slope $\dot{\gamma}\tau/2$. The velocity reduction inside the globule reflects flow stagnation. (c) The velocity in the z direction v_z taken from a straight contour that is parallel to the x axis and goes through the center of mass of the chain. The full curve is the calculated velocity profile. The long dashed curve corresponds to the rotational velocity of a sphere in shear flow with a slope of $\dot{\gamma}\tau/2$. Notice that in this case the fluid velocity in the absence of the chain vanishes.

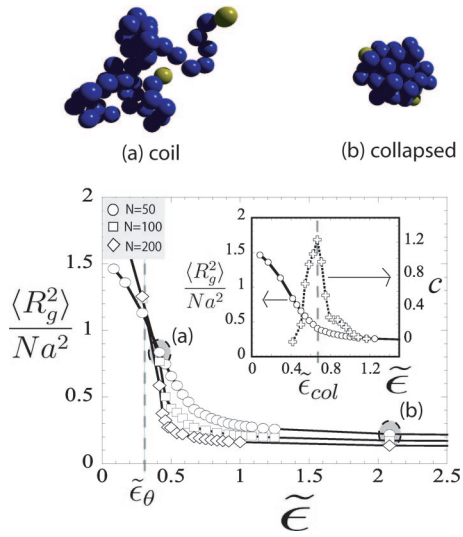

Figure 2. Rescaled radius of gyration R_g^2/Na^2 as a function of the attraction strength $\tilde{\epsilon}$ in the absence of shear for three different chain lengths. The inset shows data for $N = 50$ together with the curvature $c = \partial^2\langle R_g^2/Na^2\rangle/\partial\tilde{\epsilon}^2$. The θ point and the maximum curvature point are located at $\tilde{\epsilon}_\theta = 0.314$ and $\tilde{\epsilon}_{col} = 0.66$, respectively. (Top) Snapshots of the polymer at two different values of $\tilde{\epsilon} = 0.41$, 2.08 as indicated by shaded circles in the data for $N = 50$. Notice that for $\tilde{\epsilon} = 0.41$ the chain is between the θ-temperature and the maximum-curvature point and does not appear to be collapsed.

This heuristic definition gives a robust geometric measure of the transition from a compact object to a loose "random walk" structure. This can be seen from the snapshots provided in Figure 2, where a polymer below the θ point still resembles a coiled polymer, while above $\tilde{\epsilon}_{col}$ the polymer is definitely in a compact state. As an example, for a polymer with $N = 50$ we find $\tilde{\epsilon}_{col} \sim 0.66$, in close agreement with previous simulation studies where the specific heat was used to estimate the transition point.[22] Recently, other groups have characterized the collapse transition by computing the specific heat with the use of Ferrenberg−Swendsen reweighting techniques. Their results are very close to ours even though the polymer models are somewhat different.[23,25]

B. Shear-Induced Unfolding. A polymeric globule in shear flow displays two dynamical regimes: for low shear rates the chain remains in a compact state, while above a critical shear rate denoted by $\dot{\gamma}^*$ the polymer undergoes sudden and repeated globule−stretch transitions. The polymer does not remain in the elongated configuration because this state is unstable in simple shear flow.[7] This is similar to swollen coils, where the so-called tumbling dynamics of individual DNA molecules in shear flow has been directly observed.[2,3]

An example of this behavior is shown in Figure 3 where we show snapshots of a collapsed polymer ($\tilde{\epsilon} = 2.08$) at a shear rate $\dot{\gamma}\tau = 1.2$ slightly above the unfolding threshold (which according to a criterion explained below occurs at $\dot{\gamma}\tau \sim 1.1$). The upper row displays the formation of a protrusion (encircled beads) that eventually leads to a stretch−fold event. Below the snapshots we present time sequences of the extension R_s (defined as the projected polymer extension along the flow direction, see snapshots) for three different shear rates. The extension R_s is measured directly in experiments with fluorescently labeled polymers[2,4] and thus comparison of our time sequences with experimental data should in principle be possible. From the sequences it is posible to discern both dynamical regimes described above: for a small shear rate $\dot{\gamma}\tau = 0.5$ (black trace in the first sequence) the chain remains collapsed, in contrast to an uncollapsed polymer $\tilde{\epsilon} = 0.416$ (light gray curve in upper sequence) where strong length fluctuations are observed. As the shear rate $\dot{\gamma}$ is increased to $\dot{\gamma}\tau = 1.2$, the chain starts exhibiting pronounced and repeated globule−stretch events followed by folding events (as discussed before). This is shown in the middle panel and the snapshots, which are taken from the peak enclosed in the dashed rectangle. Further increase of the shear rate to $\dot{\gamma}\tau = 5.0$ simply leads to a higher frequency of stretching events. At this point it is important to note that the characteristic duration of a globule−stretch event, as well as the periodicity of stretch events is much larger than the typical rotation period $T_{rot} = 4\pi/\dot{\gamma}$. For all shear rates shown in Figure 3 one thus has T_{rot}/τ of the order of unity, while the stretch events occur with a periodicity that is at least 10 times longer.

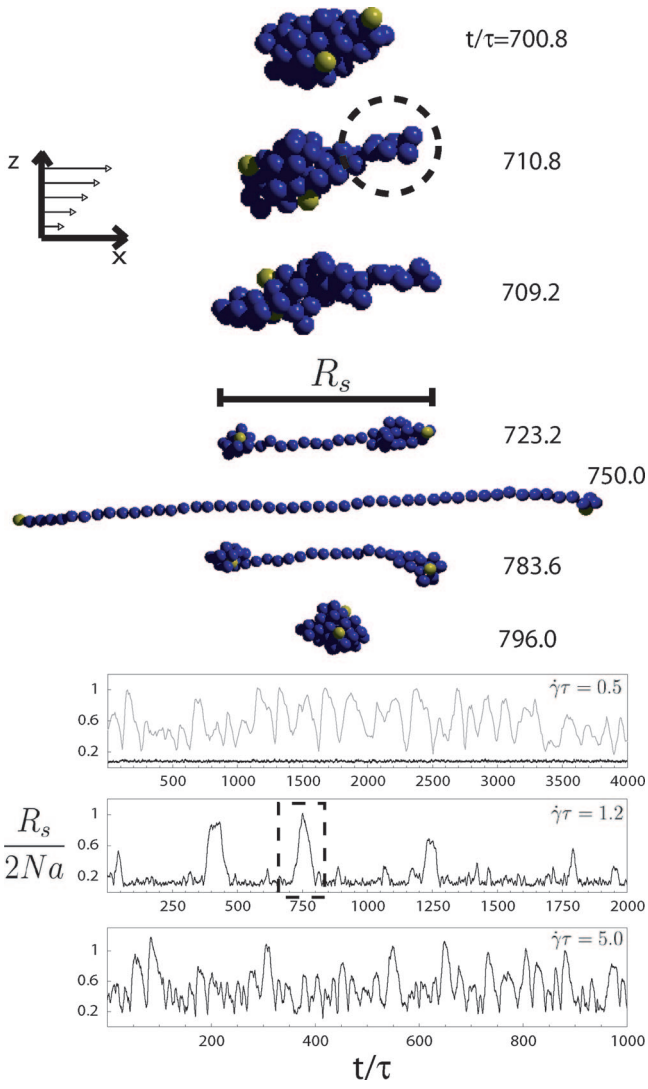

Figure 3. (Top) Snapshots of a polymer with $N = 50$ and $\tilde{\epsilon} = 2.08$ undergoing stretch−folding events at a dimensionless shear rate of $\dot{\gamma}\tau = 1.2$. The unfolding of the polymer is initiated by the formation of a small protrusion (encircled beads), which acts as a nucleus for the complete unravelling of the chain. (Bottom) Typical sequences of the extension R_s as a function of time for the free-draining case for $\tilde{\epsilon} = 2.08$ and shear rates $\dot{\gamma}\tau = 0.5, 1.2, 5$. For comparison, we also show data for $\dot{\gamma}\tau = 0.5$ for an uncollapsed polymer with $\tilde{\epsilon} = 0.416$ (light gray curve). The dashed rectangle denotes the stretching event from which the snapshots were taken.

The dynamics described before also leads to changes in the average values of all observable quantities. In Figure 4a we show the mean extension $\langle R_s \rangle$ for a chain with $N = 50$ as a function of the dimensionless shear rate $\dot{\gamma}\tau$ for different values of the attraction strength $\tilde{\epsilon}$. FD and HI simulations are distinguished by open and filled symbols, respectively. As seen, a collapsed chain undergoes a transition to an extended state beyond a threshold shear rate $\dot{\gamma}^*$ in both models, and this transition sharpens as the cohesive strength increases. For comparison, the data for an uncollapsed polymer with $\tilde{\epsilon} = 0.41$, open squares, exhibits merely a smooth unfolding crossover. The transition point $\dot{\gamma}^*$ is defined by the maximum of the "variance" of the squared chain stretching, $m = (\langle R_s^4 \rangle - \langle R_s^2 \rangle^2)/\langle R_s^2 \rangle^2$. The behavior of m for the different cohesive strengths and shear rates investigated here is shown in Figure 4b. Notice that m displays a well-defined peak at a particular shear rate in the case of collapsed polymers, while for a coiled chain (open squares) this quantity does not exhibit any characteristic change. Also, note that the peaks are smaller in the HI case, which

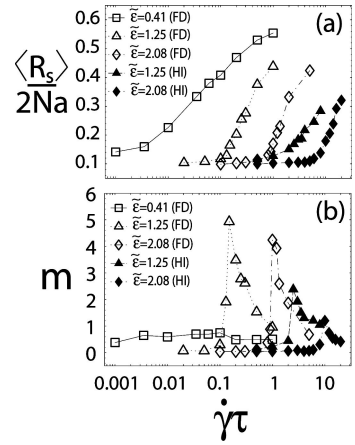

Figure 4. (a) Rescaled chain extension $\langle R_s \rangle/2Na$ for chain length $N = 50$ and different cohesive strengths $\tilde{\epsilon}$ with (HI, filled symbols) and without hydrodynamic effects (FD, open symbols) as a function of the rescaled shear rate $\dot{\gamma}\tau$. (b) The rescaled variance m of the squared polymer extension R_s^2 (see text for details) for the same cohesive strengths as in part (a). From the maximum of m the shear-induced unfolding transition is deduced.

implies that the transition is not as abrupt compared to the FD case. Nonetheless, there exist well-defined peaks for all values of $\tilde{\epsilon}$ studied in this work.

C. Protrusion Nucleation Theory. The unfolding of polymeric globules in shear flow can be understood by a simple nucleation model based on the presence of thermally excited polymeric protrusions, i.e., short polymer strands that protrude out from the globule boundary into the surrounding solvent.[11] The view that protrusions must play an important role in the destabilization of polymeric globules is supported by three distinct observations: (i) First of all, in the simulations we do observe that protrusions always precede the unfolding of globules (note that not all protrusions lead to globule unfolding, most of them in fact disappear after a short lifetime); see the snapshots of Figure 3. (ii) As has been shown by Taylor in a series of classical papers, spherical fluid drops are stable with respect to arbitrarily high shear rates if the ratio of inside and outside viscosities exceeds 4.[17] It is self-evident that the viscosity of a polymeric globule is much higher than that of the surrounding solvent, and therefore the standard hydrodynamic theory of drop stability predicts polymeric globules not to unfold in shear, in sharp contradiction to the simulation results. (iii) Finally, the simulation results for the critical shear rate for globule unfolding depend both on temperature and on the monomer radius, in sharp contrast to standard hydrodynamic instability theories. All these facts together strongly suggest a fluctuation-dominated mechanism for globule unfolding that involves fluctuations on the microscopic length scales (i.e., at the lower spatial cutoff).

To illustrate our scaling theory in a simple geometry we consider first a planar interface under shear and later investigate spherical polymer globules.

1. Instability of a Planar Polymeric Melt Fluid Interface in Shear. Here, we analyze the stability of a polymer melt−solvent interface in shear flow (see Figure 5). In particular, we are interested in determining the critical shear rate at which chain pullouts are frequently observed, which we take as an indication that the interface becomes unstable. We will later use the same approach and apply it to spherical polymer globules. It is important to note that we are not considering the free energy of a chain that is pulled out by the shear; rather, we construct a nucleation argument that identifies the critical shear rate as the one where the hydrodynamic drag is large enough to

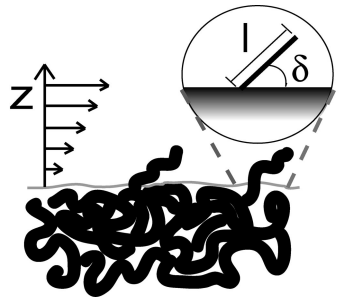

Figure 5. Schematic illustration of protrusions at an interface between a polymer melt (bottom) and a simple fluid (top) under shear. Activated by thermal energy, polymer ends stick out from the polymer melt and dangle into the fluid phase, where they are subject to hydrodynamic shear forces. The enclosed circle contains an amplification of a single protrusion of length l that forms an angle δ with the surface.

overcome the cohesive force pulling a protrusion back into the polymeric melt phase.

To proceed, we assume the interface to be flat and exhibit thermally excited protruding polymer segments of length l which form an angle δ with the surface, as shown in Figure 5. We neglect hydrodynamic interactions within the polymer and between neighboring protrusions, which is justified because the no-slip surface screens hydrodynamic interactions.[26] In our scaling approach, we assume that the shear force acts on spontaneously created protrusions. So we first have to estimate the length of a thermal protrusion. The cohesive force f_{coh} pulls protrusions back into the polymer phase and is given by

$$f_{coh} \sim \Delta\epsilon/a \tag{6}$$

where $\Delta\epsilon/a^2$can be regarded as an effective surface tension, and a corresponds to the monomer size. Assuming the cohesive force to be independent of the protrusion length amounts to the case of a sharp interface. Later, in the case of spherical globules in shear, we will lift that restriction and also consider diffuse interfaces. Due to thermal equipartition, the characteristic protrusion length l follows as

$$l \sim k_B T/f_{coh} \sim k_B T a/\Delta\epsilon \tag{7}$$

The hydrodynamic drag on the protruding segment acts parallel to the surface and results by integrating the shear force along the contour. It is given by

$$f_{prot} \sim \dot{\gamma} l^2 \sin(\delta)/(\mu_0 a) \tag{8}$$

where μ_0 denotes the Stokes mobility of a single monomer of size a. The force component along the protrusion contour follows as

$$f_{prot}^{\parallel} \sim \dot{\gamma} l^2 \sin(\delta)\cos(\delta)/(\mu_0 a) \tag{9}$$

By comparing the cohesive force f_{coh} and protrusive force $f_{prot}^{\parallel}$ and inserting the characteristic protrusion length eq 7 we arrive at the critical nucleation shear rate

$$\dot{\gamma}^* \sim \frac{\mu_0(\Delta\epsilon)^3}{(k_B T a)^2 \sin(\delta)\cos(\delta)} \tag{10}$$

Note that this threshold simply gives the threshold shear at which the drag force on an already existing protrusion is larger than the restoring cohesive force. The protrusion orientation is a second degree of freedom that is thermalized. Again invoking the equipartition theorem, we enforce the torque acting on the protrusion to be of order $k_B T$, i.e., $f_{prot}^{\perp} l \sim k_B T$. Using $f_{prot}^{\perp} \sim f_{prot}\sin(\delta)$, we obtain

$$\sin^2(\delta) \sim \frac{\mu_0 a k_B T}{\dot{\gamma} l^3} \tag{11}$$

Inserting this into eq 10 and using the characteristic protrusion length l from eq 7 we finally arrive at

$$\dot{\gamma}^* \sim \frac{\mu_0(\Delta\epsilon)^3}{(k_B T a)^2} \tag{12}$$

where we assumed the angle δ to be small. One notices the strong dependence of the threshold shear rate on temperature T and on the monomer size a, which shows that the present instability mechanism is distinct from the ordinary Kelvin−Helmholtz instability which does not explicitly involve temperature and a small-distance cutoff. To connect our result with previous hydrodynamic instability considerations, we define a surface tension as $\sigma = \Delta\epsilon/a^2$ which is nothing but the cohesive energy divided by the monomer area. As a function of σ, and putting in the definition of the monomer mobility $\mu_0 = 1/(6\pi\eta_s a)$, the resulting eq 12 can be rewritten as

$$\dot{\gamma}^* \sim \frac{\sigma^3 a^3}{(k_B T)^2 \eta_s} \tag{13}$$

This form is quite instructive, since it shows that for fixed surface tension σ and solvent viscosity η_s the critical shear rate is smallest for small-scale protrusion characterized by a small radius a. This means that small-scale protrusions will first destabilize the interface. The lowest possible value of a and thus of the critical shear rate is set by the molecular size of the polymeric material. This clearly demonstrates that the present instability mechanism is fundamentally different from an ordinary hydrodynamic instability. Let us put in explicit numbers: for water as a solvent with $\eta_s = 10^{-3}$ Pa·s, $\Delta\epsilon \simeq k_B T$, and $a \simeq 1$ nm, the critical shear rate is of the order of $\dot{\gamma}^* \simeq 10^8$ s^{-1}; i.e., the shear rate needed to overcome cohesive forces is enormous. This explains why for normal liquid–liquid interfaces the present mechanism is largely irrelevant. Only for highly viscous media, where the normal Kelvin−Helmholtz mechanism is preempted, or for small cohesive energies, will the microscopic instability discussed here be operative.

It is important to keep in mind that the present argumentation is analogous to nucleation theory and defines the critical shear at which the cohesive force is weaker than the destabilizing shear force for a typical protrusion length. Even below that critical shear rate, few polymers will be pulled out from time to time when they protrude sufficiently out from the interface, but these events are rare and thus do not represent the typical behavior.

Similar calculations for the shear force acting on a surface-grafted polymer in good solvent have appeared in the literature.[27] Those calculations were done for a long polymer, in which case the separation from the surface is not dominated by angular fluctuation (as in our case) but rather by steric interactions between the polymer and the substrate. There is a protrusion length dependent crossover between our results and those in,[27] but we note that for the present case of thermally created protrusions the short-length limit considered here is the relevant one.

2. Instability of Spherical Globule in Shear. For the case of a collapsed polymer we approximate the globule shape as a sphere of radius R, and calculate the hydrodynamic drag force f on a protruding polymer segment of length l. We assume the protrusion to be small compared to the radius R, and thus it will not influence strongly the hydrodynamic field around the rotating compact globule. The location and orientation of the protrusion in this case is important; to simplify the discussion, we focus only on the two most relevant cases (see Figure 6):

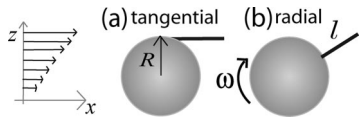

Figure 6. Sketch of two typical configurations of protrusions of length l for a spherical globule of radius R which is rotating in shear flow.

(a) a tangential protrusion at the north pole where the tangential drag is the largest, and (b) a radial protusion at an angle of $\pi/4$ that corresponds to the angle of maximum radial drag. A particularly simple case is the calculation of the drag force in the tangential configuration for the free draining (FD) case. First we note that in both hydrodynamic scenarios, FD or HI, a sphere rotates in shear flow at an angular velocity of $\omega = \dot{\gamma}/2$ (see also Figure 1). This result simply states that the total torque on the sphere is zero. The velocity of the fluid within the FD approximation at the north pole (measured with respect to the center of mass of the polymer) is $v_x \sim \dot{\gamma}R$, and thus the drag force on a segment of length l in this case is given by

$$f_{\text{prot}} \sim \dot{\gamma} lR/(\mu_0 a) \tag{14}$$

The radial pulling force in the $\pi/4$ configuration leads to the same scaling result apart from a different numerical prefactor. In the hydrodynamic case there is no slip at the globule−solvent boundary and the difference between solvent and sphere velocity gradually increases away from the sphere surface. In this case, the force has to be integrated along the contour of the protruding segment for the particular velocity field around the globule. Fortunately, the velocity field around a sphere in shear flow has been calculated exactly and is given by[28]

$$v_\alpha = \dot{\gamma} z \delta_{\alpha,x} + \frac{\dot{\gamma}R}{2}\left(\frac{5(1-(r/R)^2)\alpha\, xz}{R^3(r/R)^7} - \frac{\delta_{\alpha,z}x + \delta_{\alpha,x}z}{R(r/R)^5}\right) \tag{15}$$

where $\alpha = x, y, z$, and $r^2 = x^2 + y^2 + z^2$. Inside the sphere the flow is only rotational with an angular velocity $\omega = \dot{\gamma}/2$ as explained before.

The force on a protrusion is then given by

$$f_{\text{prot}} = (1/\mu_0)\int_0^l (\vec{v} - \vec{v}_0)\cdot(\vec{dl}/a) \tag{16}$$

where $\vec{v}_0$ is the reference velocity at the surface of the globule from where the protrusion is originating, and $\vec{dl}$ is an infinitesimal vector displacement along the contour of the segment. Since we are considering only small protrusions, the velocity field can be expanded in a Taylor series around the surface of the sphere. The particular coefficients of the expansion depend on the contour chosen. Expanding eq 15, one finds that the relative solvent velocity away from the globule surface grows as $v_r \sim \dot{\gamma} r^2/R$, where r is the distance coordinate away from the sphere surface. This functional form leads to a hydrodynamic force given by

$$f_{\text{prot}} \sim \dot{\gamma} l^3/(a\mu_0 R) \tag{17}$$

Note that the functional dependence on the sphere radius is changed in the hydrodynamic case when compared to the free draining result eq 14. The larger the sphere radius, the smaller the drag in the hydrodynamic case, see eq 17, while in the free-draining case the drag increases with increasing sphere radius. This can be easily understood since in the hydrodynamic case the no-slip boundary condition on the sphere surface leads to a screening of the shear flow around the rotating sphere, which is more pronounced the bigger the sphere is. In the free draining case, on the other hand, there is no screening and the bigger the sphere radius the larger the solvent velocity at the sphere perimeter is.

Apart from the hydrodynamic drag force, there is a restoring force acting on the protrusion due to the cohesion among monomers and due to the configurational entropy loss of a polymer in an extended configuration. In our particular case for a collapsed polymer, we assume the restoring force on a protrusion to be linear in $\tilde{\epsilon}$ and to scale as

$$f_{\text{coh}} \sim \frac{k_B T}{a}\Delta\tilde{\epsilon}(l/a)^{\alpha-1} \tag{18}$$

where the shift in the interaction parameter $\Delta\tilde{\epsilon} = (\tilde{\epsilon} - \tilde{\epsilon}_{\text{col}})$ accounts for the configurational entropy loss in the globule. In other words $[(k_B T)/a^2]\Delta\tilde{\epsilon}$ corresponds to an effective "surface tension" that tends to zero as the collapse transition is approached. We note that any nontrivial power-law behavior on $\Delta\tilde{\epsilon}$ is neglected, so our scaling form is only valid relatively far away from the critical collapse transition. Note that we consider a slightly more general form for the cohesive force than in the planar geometry, eq 6, that has two interesting limits: for a protrusion much longer than the globule−solvent interfacial width, one expects $\alpha = 1$ and thus a constant cohesive force not depending on the protrusion length. For a protrusion that is shorter than the interfacial width one expects $\alpha = 2$ in the harmonic approximation. We note that our expression for the coheisve force with $\alpha = 1$ is equivalent to the well-known critical force for unwinding collapsed polymers.[9,10]

From the equipartition theorem the typical protrusion length l follows (similar to the previous analysis for a planar interface) as

$$l \sim k_B T/f_{\text{coh}} \sim a\Delta\tilde{\epsilon}^{-1/\alpha} \tag{19}$$

Finally, by comparing the hydrodynamic drag f_{prot} from eq 17 (which tends to elongate protrusions), with the cohesive force f_{coh} from eq18 (which pulls protrusions back into the globule), and inserting the typical protrusion length into both expressions, one obtains for the threshold shear rate $\dot{\gamma}^*$:

$$\dot{\gamma}^*\tau \sim \begin{cases} \Delta\tilde{\epsilon}^{2/\alpha} a/R & \text{(FD)} \\ \Delta\tilde{\epsilon}^{4/\alpha} R/a & \text{(HI)} \end{cases} \tag{20}$$

It is important to notice that the dependence on the globule radius R is opposite when hydrodynamic effects are included. In the HI case the critical shear rate increases as R grows, since a larger sphere leads to a reduced fluid shear rate at its surface.[28] Note that in the planar calculation leading to eqs 12 and 13 there is no analogous distinction between free-draining and hydrodynamic scenarios and that the dependence on the cohesive energy parameter $\Delta\epsilon$ is intermediate between the FD and HI cases in eq 20 for $a = 1$. Note also that the hydrodynamic drag force in the planar case, eqs 12 and 13, does not follow from the drag force result in the spherical geometry (eq 20) by considering the limit of vanishing curvature $R \to \infty$. This means that an infinitely large sphere in shear does not correspond to the Couette geometry shear between two planar boundaries. The main reason for this is that no force is acting on the sphere, in contrast to the planar walls in the Couette geometry.

Our argument identifies the critical shear rate at which the hydrodynamic drag on a typical protrusion is large enough to overcome the restoring force from monomer–monomer attractions, similar to classical nucleation theory. Global free energy arguments as used for the unfolding of a globule under external stretching force[9] are irrelevant, since a polymeric protrusion nucleus which has not reached the threshold length will be wrapped around the incessantly rotating globule and be eliminated within one period of revolution.

Our scaling analysis can be understood intuitively if one compares the potential of mean force associated with the

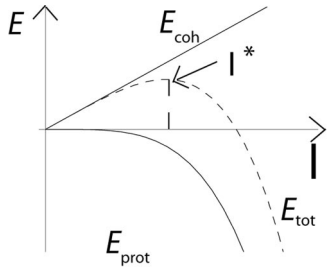

Figure 7. Plot of the destabilizing protrusion potential due to hydrodynamic drag, E_{prot}, and the stabilizing cohesive potential of mean force, E_{coh}, as a function of the protrusion length l. The total potential of mean force is denoted by the dashed curve, and displays a maximum at a length $l = l^*$.

hydrodynamic drag E_{prot} (obtained via the relation $\partial E_{prot}/\partial l = -f_{prot}$) with the potential of mean force due to cohesion E_{coh} (obtained via $\partial E_{coh}/\partial l = -f_{coh}$) From eqs 14, 17, and 18 one sees that $E_{prot} \sim -l^2$ in the free-draining case and $E_{prot} \sim -l^4$ in the hydrodynamic case, while $E_{coh} \sim l^\alpha$. These potentials are depicted in Figure 7. The total potential, which corresponds to the sum of both contributions (dashed curve), shows a maximum at some particular value l^* that depends on the shear rate $\dot\gamma$, and on the parameters R, $\Delta\tilde\epsilon$, η, and a. This point defines an instability and thus the threshold protrusion length. Conversely, it defines the critical shear rate beyond which stretching events occur frequently; for values of $l < l^*$ the protrusion will be pulled back into the globule, while for $l > l^*$ the protruding segment is dragged out of the globule. An interesting conclusion from this comparison is that the FD case with $\alpha = 2$ is a marginal point, in line with deGennes' analysis for Θ-solvent polymers.[7] Note that in the HI case the transition is always "first order" since the protrusion needs to overcome a barrier, as indeed seen in our hydrodynamic simulations.

In Figure 8a we compare our simulation results for the critical shear $\dot\gamma^*\tau$ with the scaling prediction for the FD (using $\alpha = 1$, solid line with slope –1) and HI case ($\alpha = 2$, dashed line with slope 1), confirming the different scaling dependence on globule radius in the two cases, see eq 20. In the simulation, the globule radius $\tilde R_0$ is defined as the extension in the absence of shear, i.e., $\tilde R_0 = \langle R_s/a\rangle_{\dot\gamma=0}$. Different values of α point to a sharp globule−solvent interface in the FD case (characterized by $\alpha = 1$) and a presumably hydrodynamically roughened interface in the HI case ($\alpha = 2$). Deviations of the HI data from the scaling prediction (the dotted line in Figure 8a has slope 0.69 and is a best fit to the data) are brought out more clearly in Figure 8b where we plot the rescaled critical shear rate $\dot\gamma^*\tau\tilde R_0$ for the FD case and $\dot\gamma^*\tau/\tilde R_0$ for the HI case as a function of the cohesion variable $\Delta\tilde\epsilon$. The freely draining data now exhibit two regimes, and close to the collapse transition one finds $\alpha = 2$ characteristic of protrusions shorter than the globule interfacial width, indicating a rough interface as expected, and further away from the collapse transition the data are described well by $\alpha = 1$, pointing to a sharp interface. The crossover between these regimes occurs at $\Delta\tilde\epsilon \approx 0.4$. In the limited range available for the critical shear rate, the hydrodynamic data shows behavior close to the scaling prediction; the broken line has slope 2 and corresponds to $\alpha = 2$, the dotted line has slope 1.38. Reasons for deviations are probably a break down of the simplified assumption about the spherical shape of the globule and the globule−solvent interface, which are both perturbed by hydrodynamic drag effects. These effects are considered below using a more general model that incorporates a penetration length of the solvent velocity field into the globule.

3. Partially Penetrable Globule. We next derive a general formula for the critical shear rate that interpolates between the free-draining and the nondraining regimes. The idea is to

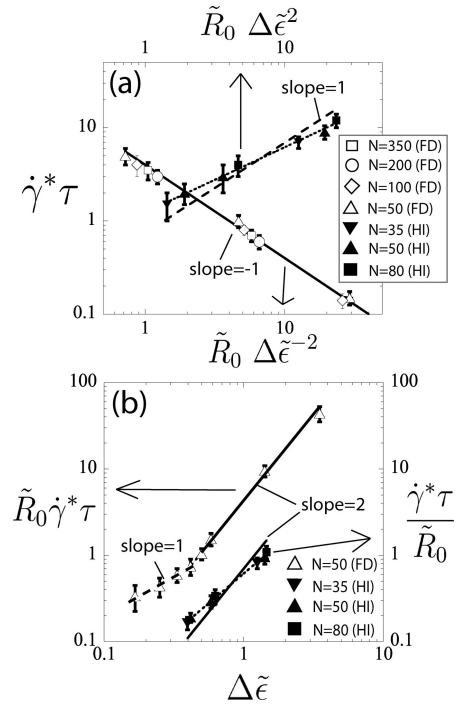

Figure 8. (a) Dimensionless critical shear rate $\dot\gamma^*\tau$ for the FD and HI case (open and filled symbols, respectively) as a function of rescaled radius according to eq 2. (b) Rescaled critical shear rate $\tilde R\dot\gamma^*\tau$ as a function of $\Delta\tilde\epsilon$ for $N = 50$ in the FD case (open triangles). The filled symbols correspond to the rescaled critical shear rate $\dot\gamma/\tau/\tilde R_0$ in the HI case. In both graphs the solid and dashed lines correspond to the scaling predictions with $\alpha = 1$ and $\alpha = 2$, respectively. The dotted lines are fits to the data, see text.

consider an effective hydrodynamic radius of the globule R_{HI} that can be smaller than the actual size R. This corresponds to a fluid flow that can partially penetrate the polymer globule boundary up to a penetration depth $\lambda = R - R_{HI}$. With this definition we see that in the limit $\lambda = 0$ we recover the HI results, while for $\lambda = R$ we recover the FD case. The derivation proceeds by considering as before the protrusion length l to be small compared to R, and by expanding the fluid velocity field in powers of l/R for a given protrusion configuration: tangential or radial. Here, we explicitly consider the tangential configuration for which the vertical coordinate is fixed at $z = R$. Starting from the exact velocity field, eq 15, that for the tangential scenario can be written as

$$v_x = \dot\gamma R + \frac{\dot\gamma R}{2}\left(\frac{5(1-(r/R_{HI})^2)x^2}{R_{HI}^2(r/R_{HI})^7} - \frac{R/R_{HI}}{(r/R_{HI})^5}\right) \qquad (21)$$

where $r^2 = R^2 + x^2$, and expanding this function in powers of x/R we arrive at

$$v - v_0 = \frac{\dot\gamma R}{2}\Big((1-(1-\lambda/R)^5) - 5(1-\lambda/R)^3\Big(1-\frac{3}{2}(1-\lambda/R)^2\Big)(x/R)^2\Big) \qquad (22)$$

Integrating over the contour length and inserting the typical protrusion size $l \sim a\Delta\tilde\epsilon^{-1/\alpha}$ finally yields the critical shear rate

$$\dot\gamma^*\tau \sim \dot\gamma^*_{FD}\tau\left((1-(1-\lambda/R)^5) - \frac{5(1-\lambda/R)^3}{3}\Big(1-\frac{3}{2}(1-\lambda/R)^2\Big)\left(\frac{a}{R}\right)^3(\dot\gamma^*_{FD}\tau)^{-1}\right)^{-1} \qquad (23)$$

where $\dot\gamma^*_{FD}\tau = \Delta\tilde\epsilon^{2/\alpha}a/R$ corresponds to the previously obtained critical shear rate for the FD case. It is important to notice the

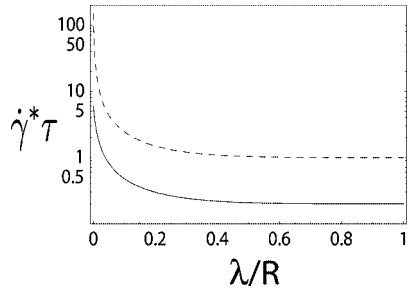

Figure 9. Dimensionless critical shear rate $\dot{\gamma}\tau$ as a function of λ/R, where λ corresponds to the penetration length of the flow. The radius in both curves has been fixed to $R/a = 5$, and $\Delta\tilde{\epsilon} = 1$ (solid line), $\sqrt{5}$ (dashed line). The limiting values of the two curves as $\lambda/R \to 0$ are $\dot{\gamma}\tau \to 6$, 160 for $\Delta\tilde{\epsilon} = 1$, $\sqrt{5}$ respectively.

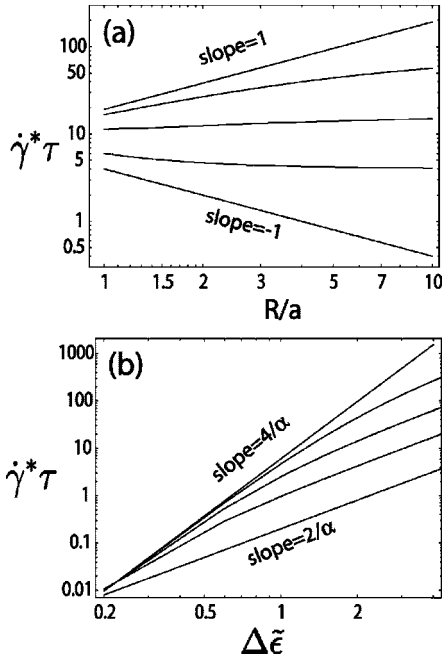

Figure 10. (a) Dimensionless critical shear rate $\dot{\gamma}^*\tau$ as a function of R/a for fixed $\Delta\tilde{\epsilon} = 2$. The different lines correspond to $\lambda/R = 0$,0.002, 0.01, 0.04, 1 from top to bottom, and $\alpha = 1$. The limiting cases $\lambda/R = 0$ (hydrodynamic nondraining limit) and $\lambda/R = 1$ (free draining limit) lead to slopes $+1$ and -1, respectively. (b) The dimensionless critical shear rate $\dot{\gamma}^*\tau$ as a function of $\Delta\tilde{\epsilon}$ for a fixed radius $R/a = 5$. The different lines correspond to $\lambda/R = 0$, 0.002, 0.01, 0.04, 1 from top to bottom. The value of α used to compute these curves is $\alpha = 1$. The limiting cases $\lambda/R = 0$ (hydrodynamic nondraining limit) and $\lambda/R = 1$ (free draining limit) lead to slopes $4/\alpha = 4$ and $2/\alpha = 2$, respectively.

strong dependence on the penetration length λ in eq 23. This can be clearly seen in Figure 9 where we plot $\dot{\gamma}^*\tau$ as a function of λ/R, for two values of $\dot{\gamma}^*_{FD}\tau$ and one value of R comparable to that used in the simulation. Notice that for very small variations of λ in the nondraining limit of our theory ($\lambda = 0$), the critical shear rate changes dramatically. Also, notice that this effect is accentuated for higher values of $\Delta\tilde{\epsilon}$, and that the FD result is quite robust for values down to $\lambda/R \sim 0.15$.

Apart from understanding the dependence of $\dot{\gamma}\tau$ on λ/R, it is important to figure out how the scaling of the critical shear rate with the physical values $\Delta\tilde{\epsilon}$ and R depends on λ. This is shown in Figure 10, where in (a) we fix the monomer–monomer effective interaction potential $\Delta\tilde{\epsilon} = 2$, and consider variation on R, and in (b) we fix $R = 5a$ (close to our simulation values) and vary $\Delta\tilde{\epsilon}$. The change in the R dependence is sensitive to extremely small variations of λ/R. Nonetheless, the characteristic ratio λ/R depends on the chain length N via the sphere radius as $R \sim N^{1/3}$, so that in our simulations we can only asses a very small range of radii, particularly when considering the numerically demanding HI case. In part (b) we note that also the scaling dependence of $\dot{\gamma}\tau$ on $\Delta\tilde{\epsilon}$ changes dramatically as λ/R deviates slightly from the asymptotic HI case. This might be the reason why our HI simulation results do not yield the HI scaling, because in simulations one always expects partial flow penetration. Particularly for $\Delta\tilde{\epsilon} > 2$ one seems to obtain FD scaling even for $\lambda/R \ll 1$.

D. Spectral Properties. The spectral properties of the dynamics of the end-to-end vector, or the stretch $R_s(t)$, are of interest because they are related to dissipation in the system and demonstrate how shear affects the different polymeric fluctuation modes. Interestingly, it has been observed that for noncollapsed polymers the R_s spectrum is very similar for simulations that use hydrodynamic interaction and those which do not incorporate them.[1] This point is reproduced below. Also, it has been shown that noncollapsed polymers can be efficiently represented by elastic dumbbells with friction coefficients that depend on the specific model and the particular interactions among the monomers. This mapping has been very useful since simple polymer models can thus be used to understand and predict the rheological behavior of polymer solutions.[29]

Here we analyze the power spectral density (PSD) $P(\omega)$ of the polymer stretching radius R_s since this quantity can be measured directly by experiments. The PSD for R_s is given by

$$\mathcal{P}(\omega) = R_s(\omega)R_s^*(\omega) \tag{24}$$

where $R_s(\omega)$ is the spectral representation of the time sequence of $R_s(t)$, i.e.

$$R_s(\omega) = \int_0^T R_s(t)e^{-i\omega t}dt \tag{25}$$

and $R_s^*(\omega)$ is the complex conjugate. Notice that the inverse Fourier transform of the $P(\omega)$ is the real time correlation function. In order to obtain the different power spectral distributions, we performed long simulations. Subsequently, the trajectories were divided in n equal sized time domains, and a fast Fourier transform was taken of each of these individual time sequences. Finally, all the $P(\omega)$'s resulting from the previous step were averaged to yield the results displayed in the figures. The interval used in the transforms is simply $T/\tau = 2\pi/(\omega_0\tau)$, where $\omega_0\tau$ correspond to the lowest frequency point shown in the graphs.

For noncollapsed polymers at relatively high shear rates it has been observed by several groups in experiments and simulations that the $P(\omega)$ shows three different regimes. At small frequencies it displays a plateau, while for intermediate frequencies the spectrum decays with a power close to 3.6.[1,2] For high frequencies the decay power becomes closer to 2. The time scale that determines the boundaries in this case is the polymer relaxation time. For $\dot{\gamma} = 0$ it has also been observed that the $P(\omega)$ corresponds to that of a simple harmonic spring. In Figure 11 we show our $P(\omega)$ results for a polymer with $N = 50$ near the θ point. As can be clearly seen from the graph, both hydrodynamic scenarios, free-draining and nondraining, exhibit the same behavior (apart from a time constant), and they are in excellent agreement with previous results summarized in ref 1. In particular, one can see from Figure 11a that at zero shear $\dot{\gamma} = 0$, the chain behaves like a simple harmonic oscillator, and the $P(\omega)$ is well fitted by a function of the form $P(\omega) = a_1/(1 + a_2(\omega\tau)^2)$ (solid curve), where a_1 and a_2 are fitting parameters. This equation is nothing but the response function of a simple Hookean spring when inertial effects can be neglected. As the shear rate increases but remains low, the scaling region over which $P(\omega)$ scales as $P(\omega) \sim (\omega\tau)^{-2}$ becomes larger. Finally, for strong stretching the polymer displays a plateau followed

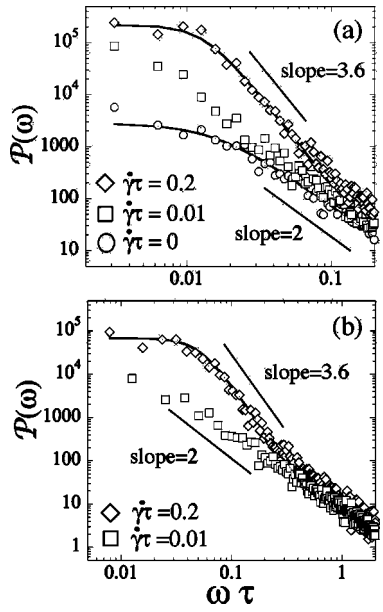

Figure 11. Power spectral density P(ω) for a noncollapsed polymer ($\tilde{\epsilon}$ = 0.41 and N = 50) for two hydrodynamical regimes: (a) free-draining, and (b) including hydrodynamic interactions. The different symbols correspond to different shear rates, as indicated in the figure. The solid lines in part (a) are fits using a functional form $P(\omega) = a_1/(1 + a_2(\omega\tau)^b)$, with b = 3.6 (upper curve) and b = 2 (lower curve). In part (b) the solid line that goes through the data for not too high frequencies is also a fit using the same functional form as in part (a) with b = 3.6.

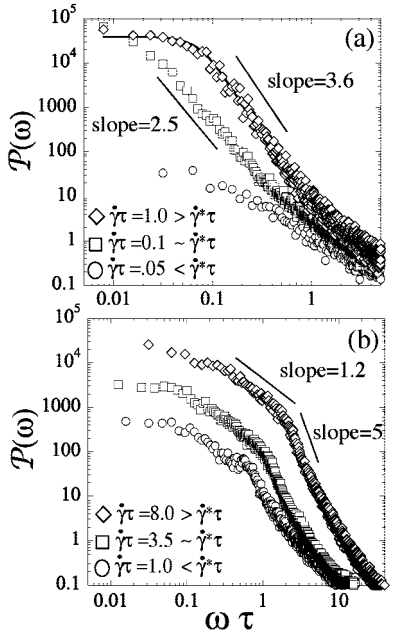

Figure 12. Power spectral density P(ω) for a globular polymer ($\tilde{\epsilon}$ = 1.25) for two hydrodynamical regimes: (a) free-draining, and (b) including hydrodynamic interactions. The different symbols correspond to different shear rates, as indicated in the figure. The solid line that goes through the data in part (a) is a fit using the same functional form as in Figure 11 with b = 3.6.

by a decay with a power ~ -3.6 that levels out eventually to a power similar to ~ -2. The behavior changes very little when one includes hydrodynamic interactions, as shown in Figure 11b.

On the other hand, the situation is completely different for collapsed chains. In this case, both hydrodynamic scenarios give qualitatively different results as can be seen in Figure 12. While the FD scenario eventually leads to a behavior similar to the one displayed by noncollapsed polymers (see Figure 12a), the HI case exhibits a qualitatively different spectrum (Figure 12b). In particular, we see that the PSD decays in a finite frequency window rather slowly with a slope of approximately $P(\omega) \sim (\omega\tau)^{-1.2}$, and this behavior persists even for very high shear rates. Our results thus suggest that hydrodynamic effects are especially important in determining the dynamics of collapsed polymer chains under shear.

E. Shear Viscosity. In this subsection we analyze the shear viscosity of globular polymers in flow. Our analysis is based on single-polymer simulations and thus valid only for dilute solutions where interactions between globules can be neglected. Note that in large shear it has been noted that gelation occurs in polymer systems with attractive interactions beyond a threshold shear rate.[30] In the case of the vWF, it has been also observed that under some shearing conditions it can form a 3D weblike structure[31] or simply large aggregates.[32]

To calculate the viscosity we directly evaluate the contribution per polymer to the stress tensor π as[29,33]

$$\boldsymbol{\pi} = \frac{c}{N}\sum_{i=1}^{N}\langle \mathbf{r}_i\mathbf{F}_i\rangle \tag{26}$$

where c is the monomer density and $\mathbf{F}_i = -\nabla_{\mathbf{r}i}U$ is the force acting on the ith bead. The average is done over the time trajectory of the simulation. The contribution of the polymer to the shear viscosity is then simply evaluated via

$$\eta^{\mathrm{p}}(\dot{\gamma}) = \frac{\boldsymbol{\pi}_{xz}}{\dot{\gamma}} \tag{27}$$

Here we use an equivalent dimensionless quantity $\tilde{\eta}$ that we define as

$$\tilde{\eta} = \frac{N\eta^{\mathrm{p}}}{6\pi\varphi\eta_{\mathrm{s}}} \tag{28}$$

where η_{s} and $\varphi = ca^3$ correspond to the viscosity of the pure solvent and the volume fraction of polymer, respectively. From the definition of the intrinsic viscosity [η], one sees that $\tilde{\eta} \sim N[\eta]$. A graph of $\tilde{\eta}$ for different values of N in the coiled ($\tilde{\epsilon}$ = 0.41) and collapsed ($\tilde{\epsilon}$ = 2.08) regimes is shown in Figure 13. For coiled polymers (Figure 13a), notice that for small shear rates the HI result is below the FD case. This suggests that we are in the large N regime, since $\tilde{\eta}$ scales differently with the index of polymerization N in the FD and HI cases. In particular, the viscosity scales in the limit $\dot{\gamma} \to 0$ as $\tilde{\eta} \sim N$ in the FD or Rouse case, and $\tilde{\eta} \sim N^{1/2}$ in the HI or Zimm case.[33] For large values of $\dot{\gamma}$ both models should converge to the same result since the polymer is almost completely stretched (apart from the tumbling events), and thus the FD approximation becomes valid. This effect is also recovered by our simulations since both FD and HI results in Figure 13a converge toward the same values for large shear rates.

Our results for the globular polymers exhibit a different behavior. In the unphysical case of FD, the data collapse by rescaling all shear rates by the critical shear rate $\dot{\gamma}$*, and the reduced viscosity $\tilde{\eta}$ by $N^{5/3}$. The shear rate rescaling reflects the expectation that the behavior of the viscosity changes dramatically across the transition point. This is confirmed in the rescaled plot Figure 13c that shows a marked difference between the slopes of the data for shear rates below and above the transition. The particular exponent of N in this case is unphysical since the solvent is allowed to penetrate the globule. On the other hand, if one considers the HI case, one expects the viscosity correction due to the presence of the globules at small shear rates to scale as $\eta \sim \varphi$. In fact, it was shown by Einstein that the correction to the shear viscosity of a dilute solution containing spherical particles is given by $\eta = 5\varphi/2\eta_{\mathrm{s}}$,[34] a formula that Taylor subsequently refined for the case of drops

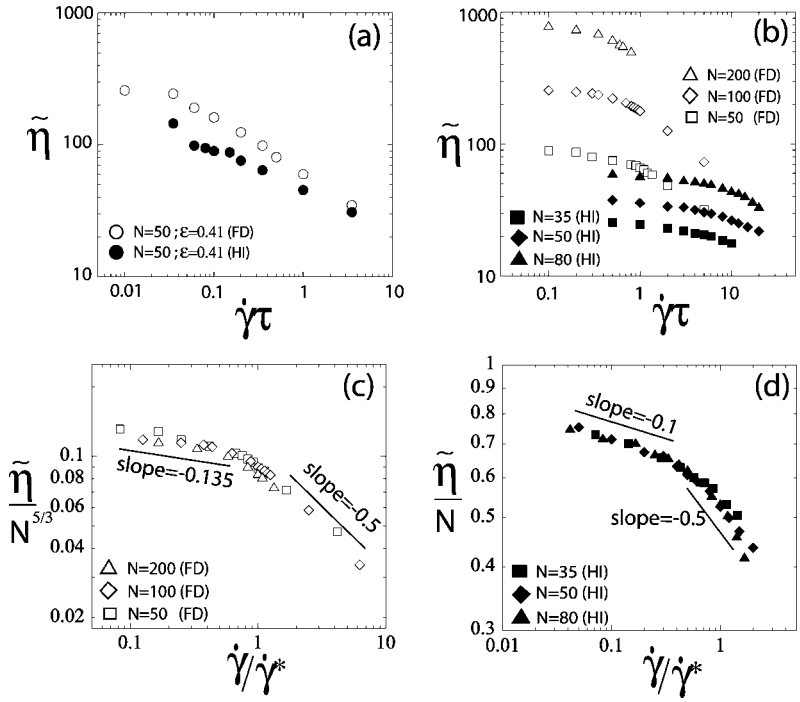

Figure 13. (a) Reduced viscosity $\tilde{\eta}$ as a function of the imposed shear rate for a noncollapsed polymer with $\tilde{\epsilon} = 0.41$ in both hydrodynamics regimes. (b) Reduced viscosity $\tilde{\eta}$ as a function of the imposed shear rate for a collapsed polymer with $\tilde{\epsilon} = 2.08$. The different symbols correspond to different polymer lengths and different hydrodynamic regimes, as indicated in the figure. (c) Rescaled reduced viscosity in FD case as a function of $\dot{\gamma}/\dot{\gamma}^*$, where $\dot{\gamma}^*$ is as before the threshold shear rate at which unfolding occurs. (d) Rescaled reduced viscosity in the HI case as a function of $\dot{\gamma}/\dot{\gamma}^*$. The different lines in the graphs have the slopes indicated in the figure.

with finite viscosity.[35] In terms of our rescaled viscosity $\tilde{\eta}$ we thus expect that the HI results should collapse when the viscosity is rescaled by the globule volume $R^3 \sim N$. The proportionality constant is a complicated quantity that depends on the interaction potential, and the internal viscoelastic properties of the globule, which most probably are changing as the shear rate is increased. Our results shown in Figure 13d for this case do in fact display this collapse. Furthermore, the proportionality constant is weakly shear rate dependent since the slope of the curve is ~0.1. Predicting this power law is not an easy task because a polymeric globule displays internal viscoelastic behavior that is sensitively modified by shear stress. For the case of a purely viscous liquid the solution by Taylor predicts vanishing slope, and the only variable is the viscosity ratio. On the other hand, it has been observed that micellar solutions[36] exhibit a viscosity that is sensitve to the shear rate in a weakly manner before rupture, similar to the behavior found by us. The region of high shear rates displays thinning behavior consistent with that found by previous works,[19,37] with a viscosity scaling as $\eta \sim \dot{\gamma}^{-1/2}$, similar to the FD case. This is understood because above the globule−stretch transition the polymers start exhibiting elongations similar to the case of noncollapsed polymers. This naturally leads to a viscosity that scales in a similar fashion. In summary, the viscosity of a dilute solution of collapsed polymer globules in shear displays a pronounced change of behavior across the unfolding transition at the critical shear rate.

IV. Final Remarks

In this paper we have supplemented the classical theories for the hydrodynamic instability of curved and planar interfaces by a protrusion-induced instability mechanism that includes thermal fluctuation effects in terms of interfacial excitations. It turns out that small-scale interface fluctuations become unstable at smaller shear rates than large-scale deformations, such that our mechanism involves the small-scale structure of the material considered and thus is very different from ordinary hydrodynamic instabilities. We have both considered spherical globules as well as planar polymeric interfaces by scaling arguments; for globules in shear we have also performed extensive hydrodynamic simulations in order to back up our scaling results.

Our studies reveal that collapsed polymers under shear flow display repetitive globule−stretch transformations above a critical shear rate $\dot{\gamma}^*$. The particular value of $\dot{\gamma}^*$ depends strongly on the attractive forces acting between monomers that are parametrized by the cohesion energy $\Delta\tilde{\epsilon}$, as well as on the size of the polymer. All our results are presented in dimensionless form, but it is also instructive to look at the scaling laws in terms of real physical quantities. First, we note that the scaling of the physical shear rate $\dot{\gamma}^*$ is given by (see eq 20)

$$\dot{\gamma}^* \sim \begin{cases} (\Delta\epsilon)^{4/\alpha} N^{-1/3} (k_B T)^{1-2/\alpha} \eta^{-1} a^{-3} & \text{(FD)} \\ (\Delta\epsilon)^{4/\alpha} N^{1/3} (k_B T)^{1-4/\alpha} \eta^{-1} a^{-3} & \text{(HI)} \end{cases} \tag{29}$$

where we use $\Delta\epsilon$ as a measure of the contact energy between two monomers. Note that both free-draining (FD) and hydrodynamic (HI) scenarios show a pronounced temperature dependence, except for the nonphysical FD case with $\alpha = 2$. For the cohesion energy, one can envision two distinct scenarios: in the first, a monomer is assumed to be a homogeneous particle with a cohesion strength proportional to the monomer surface area, i.e., $\Delta\epsilon \sim a^2\sigma$ (with σ being the surface tension, i.e., the cohesion energy per unit area), and a specific binding scenario where $\Delta\epsilon$ is treated as a parameter that is independent of the monomer size a. For the physically relevant HI case, the critical shear rate scales for both limits as

$$\dot{\gamma}^*_{HI} \sim \begin{cases} \eta^{-1} \sigma^{4/\alpha} N^{1/3} (k_B T)^{1-2/\alpha} a^{(24-9\alpha)/3\alpha} & \text{(homogeneous)} \\ \eta^{-1} (\Delta\epsilon)^{4/\alpha} N^{1/3} (k_B T)^{1-4/\alpha} a^{-3} & \text{(specific)} \end{cases} \tag{30}$$

In both cases we note that the threshold shear rate is rather insensitive to the number of monomers N, or, equivalently, to

the length of the polymer, but the dependence on the monomer size a is different in the two cases. In the case of specific monomer binding (probably more relevant for biological systems such as the von Willebrandt factor[13]), $\Delta\epsilon$ is independent of a, and thus $\dot{\gamma}^* \sim a^{-3}N^{1/3}$. Here the critical shear goes down with increasing monomer size, such that unfolding becomes more easy to achieve with bulky monomers. For the specific binding case the behavior is very different. This case is relevant to ordinary polymeric melts and possibly also to simple liquids. Here, for any value of $\alpha < 8/3$ an decrease in a leads to an decrease of the critical shear rate $\dot{\gamma}$. This means that, similar to our results shown for the planar interface case in section III.C.1, the small-scale protrusions become instable first, showing that the thermally induced shear instability is a small-scale phenomenon that starts at the lower spatial cutoff, that is, at the molecular level.

In the free-draining (nonphysical) case we obtain for both binding scenarios

$$\dot{\gamma}^*_{\mathrm{FD}} \sim \begin{cases} \eta^{-1}\sigma^{2/\alpha}N^{-1/3}(k_{\mathrm{B}}T)^{1-2/\alpha}a^{(12-9\alpha)/3\alpha} & \text{(homogeneous)} \\ \eta^{-1}(\Delta\epsilon)^{2/\alpha}N^{-1/3}(k_{\mathrm{B}}T)^{1-2/\alpha}a^{-3} & \text{(specific)} \end{cases} \tag{31}$$

Reality is somewhere in between these hydrodynamic scenarios. In particular, we note that the dependence of the critical shear rate on $\Delta\epsilon$ is quite sensitive to the penetration depth λ of the shear flow. As discussed before, even for small penetration length $\lambda/R \ll 1$, the scaling of the critical shear rate $\dot{\gamma}$ on sphere radius and cohesion strength changes radically. The scaling with the radius is difficult to access in the simulations because it involves a modest dependence on the polymerization index N. On the other hand, the scaling with $\Delta\epsilon$ is more obvious and leads to numerically significant changes. For real proteins, we expect binding sites with a distribution of different strengths. It seems plausible that this will lead to the formation of clusters that stay tightly bound at intermediate shear rates and only completely unfold at much higher shear rates. Coming back to the example of the vWF protein in the blood stream, which was the original motivation of this study, we note that with a carefully tuned effective monomer size, as well as suitable cohesive energy, unfolding can occur in a capillary that has shear rates higher than the particular critical shear rate for unfolding of that monomer size. The unraveling of the polymer will occur mostly close to the surface of a capillary where the flow gradient and thus the shear rate is maximal and where presumably the unfolding of vWf has an important physiological function.[38] Also, the wall lowers the critical shear rate even further due to a specific hydrodynamic mechanism that has recently been investigated.[39] The particular interaction among the vWF monomers is not known to this date, but we presume that it is not very high because vWF unfolds already upon adsorption to a mildly hydrophobic surface.[40] To obtain numbers, let us assume the interaction to be of the order of a typical H-bond, which is close to the simulation value $\epsilon \sim 2k_{\mathrm{B}}T$. In this case, we find $\dot{\gamma}^*\tau \approx 3R/a$ for the relevant HI case(see Figure 8b). In order for such a polymer to unfold at a typical shear rate in a human capillary of $\dot{\gamma} \sim 1000\ \mathrm{s}^{-1}$,[38] using for the viscosity of water $\eta = 10^{-3}$ Pa·s and assuming $R/a = N^{1/3}$ with $N = 100$, the required monomer radius a turns out to be of the order of $a \sim 100$ nm, which is an extremely large value when compared with normal amino acids which have a radius of less than a nanometer, but curiously it is of the right order for the vWF monomer which consists itself of a few thousand amino acids that are tightly bound.[40] Our results thus suggest that the vWF monomer is so large in order for it to unfold at physiological shear rates as found in capillary vessels. We also note that in principle the effective vWF monomers could unfold themselves. But since constituent amino acids have a much smaller radius a, and due to the a^{-3} dependence on eq 31, the shear rates are much higher for this to occur. From our scaling arguments we also understand why normal collapsed polymers and proteins, with monomers in the subnanometer range, do not show an unfolding transition upon application of even very high shear rates.[8] Assuming the same cohesion energy $\epsilon \sim 2k_{\mathrm{B}}T$ but a monomer radius of about $a \approx 0.2$ nm, the critical shear rate is of the order of $\dot{\gamma} \sim 10^8\ \mathrm{s}^{-1}$, too high for standard shearing setups.

We also formulate the protrusion-triggered nucleation argument for a planar interface between a polymer melt and a solvent. As mentioned in section III.C.1, for cohesive energies in the thermal energy range, this mechanism is irrelevant unless the viscosity of the solvent is very large (so that the classical Kelvin−Helmholtz instability mechanism would be inoperative) or the interfacial tension is low. On the other hand, our thermally activated protrusion mechanism might be important in the case of polymer melt-on-melt shearing, such as that occurring during extrusion.

With respect to the dynamical properties of polymers in shear, we demonstrated that the power spectral distribution of the polymer size is rather different between draining and free-draining scenarios. The spectral scaling changes decisively at the unfolding transition. This should be experimentally verifiable in experiments that optically track the conformational dynamics of polymeric globules in shear.

Finally, we have shown that the viscosity in the relevant HI case of dilute solutions of globular proteins or synthetic polymers exhibits an abrupt change of its viscoelastic properties close to the critical shear rate (see Figure 13d), which suggests applications as a shear-responsive nonlinear medium. We note that the low shear rate regime does not plateau and exhibits thinning for the shear rates considered. This can be explained in terms of an effective internal viscosity of the polymer that depends on the shear rate and is very different from the thinning of colloidal suspensions upon shear.[41] This demonstrates that the internal globule viscosity plays an important role for the overall viscosity of solutions of polymeric globules. The dependence on the shear rate is not very pronounced, but should be detectable for dilute suspensions. Also, it might be interesting to carefully measure the shear dependence of the viscosity of protein solutions, since that is an indirect way to learn about the effects of the internal globular viscosity, which is a topic of intense study.[42] In order to reduce the large cohesive energies for globular proteins necessary to observe shear-induced unfolding, one could combine denaturing agents (such as urea) with shear.

As a last comment, we mention that our protrusion mechanism is not restricted to polymeric systems but works in principle also for interfaces between simple liquids. In this context, it is important to note that for large cohesive energies, $\Delta\epsilon > k_{\mathrm{B}}T$, the typical protrusion length is smaller than the monomeric size a and thus our argumentation carries over without modifications to simple liquids consisting of unconnected monomeric units. However, the same restrictions and comments made for polymeric interfaces in the preceding sections also apply for simple liquids: unless viscosities are high or the interfacial tension is low, the critical shear rate for the protrusion mediated intefacial instability tends to be quite high.

Acknowledgment. The authors are grateful to M. F. Schneider for inspiring conversations. Financial support by the Bavarian Elite Fund "Complex Interfaces", via the Excellence Cluster Nano-Initiative Munich and the Deutsche Forschungsgemeinschaft (SPP1164) is acknowledged. A.A.-K. acknowledges the NSF for support through an international postdoctoral fellowship.

References and Notes

(1) Larson, R. G. *J. Rheol.* **2005**, *49*, 1.
(2) Smith, D. E.; Babcock, H. P.; Chu, S. *Science* **1999**, *283*, 1724.
(3) Schroeder, C. M.; Teixeira, R. E.; Shaqfeh, E. S. G.; Chu, S. *Phys. Rev. Lett.* **2005**, *95*, 018301.
(4) Doyle, P. S.; Ladoux, B.; Viovy, J.-L. *Phys. Rev. Lett.* **2000**, *84*, 4769.
(5) Perkins, T. T.; Smith, D. E.; Chu, S. *Science* **1997**, *276*, 2016.
(6) Schroeder, C. M.; Babcock, H. P.; Shaqfeh, E. S. G.; Chu, S. *Science* **2003**, *301*, 1515.
(7) de Gennes, P. G. *J. Chem. Phys.* **1974**, *60*, 5030.
(8) Jaspe, J.; Hagen, S. J. *Biophys. J.* **2006**, *91*, 3415.
(9) Halperin, A.; Zhulina, E. B. *Europhys. Lett.* **1991**, *15*, 417.
(10) Buguin, A.; Brochard-Wyart, F. *Macromolecules* **1996**, *29*, 4937.
(11) Alexander-Katz, A.; Schneider, M. F.; Schneider, S. W.; Wixforth, A.; Netz, R. R. *Phys. Rev. Lett.* **2006**, *97*, 138101.
(12) Schneider, S. W.; Nuschele, S.; Wixforth, A.; Alexander-Katz, A.; Netz, R. R.; Schneider, M. F. *Proc. Natl. Acad. Sci.* **2007**, *104*, 7899.
(13) Sadler, J. E. *Annu. Rev. Biochem.* **1998**, *67*, 395.
(14) Dias, C. L.; Grant, M. *Phys. Rev. E* **2006**, *74*, 042902.
(15) Szymczak, P.; Cieplak, M. *J. Chem. Phys.* **2007**, *127*, 155106.
(16) Acheson, D. J. *Elementary Fluid Dynamics*; Claredon Press: Oxford, UK, 1990.
(17) Stone, H. A. *Annu. Rev. Fluid Mech.* **1994**, *26*, 65.
(18) Rotne, J.; Prager, S. *J. Chem. Phys.* **1969**, *50*, 4831.
(19) Jendrejack, R. M.; de Pablo, J. J.; Graham, M. D. *J. Chem. Phys.* **2002**, *116*, 7752.
(20) Schroeder, C. M.; Teixeira, R. E.; Shaqfeh, E. S. G.; Chu, S. *Macromolecules* **2005**, *38*, 1967.
(21) de Gennes P. G. *Scaling Concepts in Polymer Physics*; Cornell University Press: Ithaca, NY, 1979.
(22) Zhou, Y.; Hall, C. K.; Karplus, M. *Phys. Rev. Lett.* **1996**, *77*, 2822.
(23) Parsons, D. F.; Williams, D. R. M. *J. Chem. Phys.* **2006**, *124*, 221103.
(24) Graessley, W. W.; Hayward, R. C.; Grest, G. S. *Macromolecules* **1999**, *32*, 3510.
(25) Rampf, F.; Paul, W.; Binder, K. *Europhys. Lett.* **2005**, *70*, 628.
(26) Blake, J. R. *Proc. Cambridge Philos. Soc.* **1971**, *70*, 303.
(27) Doyle, P. S.; Ladoux, B.; Viovy, J.-L. *Phys. Rev. Lett.* **2000**, *84*, 4769.
(28) van de Ven, T. G. M. *Colloidal Hydrodynamics*; Academic Press: London, 1989.
(29) Bird, R. B.; Curtiss, C. F.; Amstrong, R. C.; Hassager, O. *Dynamics of Polymeric Liquids*; Wiley-Interscience: New York, 1987.
(30) Bokias, G.; Hourdet, D.; Iliopoulos, I. *Macromolecules* **2000**, *33*, 2929.
(31) Schneider, M. F. personal communication.
(32) Shankaran, H.; Alexandridis, P.; Neelamegham, S. *Blood* **2003**, *101*, 2637.
(33) Doi, M.; Edwards, S. F. *The Theory of Polymer Dynamics*; Oxford University Press: New York, 1986.
(34) (a) Einstein, A. *Ann. Phys.* **1906**, *19*, 289. (b) Einstein, A. *Ann. Phys.* **1911**, *34*, 591.
(35) Taylor, G. I. *Proc. R. Soc., Ser. A* **1932**, *138*, 41.
(36) Buitenhuis, J.; Forster, S. *J. Chem. Phys.* **1997**, *107*, 262.
(37) Doyle, P. S.; Shaqfeh, E. S. G.; Gast, A. P. *J. Fluid Mech.* **1997**, *334*, 251.
(38) Kroll, M. H.; Hellums, J. D.; McIntire, L. V.; Schafer, A. I.; Moake, J. L. *Blood* **1996**, *88*, 1525.
(39) Alexander-Katz, A.; Netz, R. R. *Europhys. Lett.* **2007**, *80*, 18001.
(40) Siedlecki, C. A.; Lestini, B. J.; KottkeMarchant, K.; Eppell, S. J.; Wilson, D. L.; Marchant, R. E. *Blood* **1996**, *88*, 2939.
(41) Barrat, J.-L. *J. Phys.: Condensed Matter* **2003**, *15*, S1.
(42) Hagen, S. J.; Qiu, L.; Pabit, S. A. *J. Phys. Cond. Matt.* **2005**, *17*, S1503.

MA702331D